Chemical Science

ROYAL SOCIETY OF CHEMISTRY

EDGE ARTICLE

View Article Online
View Journal | View Issue

Cite this: *Chem. Sci.*, 2025, **16**, 16137

All publication charges for this article have been paid for by the Royal Society of Chemistry

Received 6th May 2025
Accepted 1st August 2025

DOI: 10.1039/d5sc03267a

rsc.li/chemical-science

Unlocking synergy between multi-valence rhodium species for promoted methanol photoreforming

Mu Xiao, [a] Weizhen Meng,[b] Yalong Jiao, [b] Haijiao Lu, [a] Zhiliang Wang, [a] Guangyu Zhao,[c] Zitong Wang,[a] Yonggang Jin[c] and Lianzhou Wang *[ad]

Solar-powered photocatalytic methanol dehydrogenation to produce hydrogen (H_2) and formaldehyde provides a promising approach for storable H_2 fuel without carbon emissions. However, the different properties of C–H and O–H bonds in methanol molecules make it challenging to cleave both bonds effectively on a single catalytic active site during the methanol dehydrogenation process. This work proposes a strategy that constructs multi-valence metal species in the co-catalyst to address this challenge. In the case study of multi-valence rhodium species (Rh^0 and Rh^{3+}) on titanium dioxide (RhO_x/TiO_2) photocatalysts, an apparent turnover frequency (TOF, the H_2 evolution rate as a function of the co-catalyst amount) of 1236 h^{-1} is achieved, outperforming that of most reported co-catalysts. Detailed investigations unveil that the synergy between Rh^0 and Rh^{3+} not only facilitates the cleavage of both C–H and O–H bonds in methanol molecules but also facilitates the desorption of H_2 molecules, leading to improved efficiency. This work showcases an effective strategy for engineering co-catalysts to promote photocatalytic methanol dehydrogenation and provides insights into the mechanism of this reaction catalyzed by heterogeneous photocatalysts.

Introduction

Methanol presents a promising liquid hydrogen carrier, due to its high hydrogen content (12.5%), facile production from renewable resources, and easy transportation and storage with well-established infrastructure.[1] In industry, methanol is converted to hydrogen (H_2) and carbon dioxide (CO_2) *via* methanol steam reforming at relatively high temperatures (250–350 °C) and pressures (10–50 bar), leading to high capital cost and high carbon emissions. Photocatalytic methanol reforming to produce H_2 and formaldehyde (CH_2O) provides a promising approach by using solar energy, abating CO_2 emissions, and operating under mild conditions.[2] Furthermore, the by-product formaldehyde is the major industrial feedstock for manufacturing cosmetic products, glues, and resins, with a considerably large market.[3] In addition, formaldehyde can generally dissolve in the reaction solutions, which simplifies the separation from H_2 gas and thus reduces additional costs.[4] Therefore, solar-driven photocatalytic dehydrogenation, as a bifunctional approach to producing storable H_2 and valuable by-products, has attracted increasing attention.[5–7]

Co-catalysts play a crucial role in semiconductor-based photocatalytic reactions, as they control the activation of reactants, thereby boosting surface reaction rates and regulating product selectivity.[8] As methanol has been commonly used as a sacrificial agent for photocatalytic water splitting to produce H_2, H_2 evolution co-catalysts (HEC) for this reaction, such as platinum (Pt), copper (Cu), nickel (Ni), and MoS_2, have been intensively explored for H_2 production from methanol.[5,9–11] Despite promising results obtained, it remains challenging to achieve energy-efficient H_2 production towards practical implementation. Unlike the two identical O–H bonds in water molecules, the different characteristics of the O–H bond and C–H bond in methanol molecules make it unfavorable to proceed with the cleavage of both bonds on a single catalytic site actively.[12–14] For instance, the dissociative adsorption of methanol ($CH_3OH \rightarrow CH_3O^* + H^*$) was shown to occur on the surface of NiO spontaneously, while the following activation of the C–H bond faced a high free energy barrier, retarding the catalytic activity.[15] In another case, the scission of the C–H bond in the methanol molecule was thermodynamically more favorable than that of the O–H bond on the surface of MoS_2.[7] Hence, the design of high-performance co-catalysts for efficient methanol dehydrogenation remains an unsolved puzzle.

Herein, we report the design of co-catalysts that are composed of multi-valence metal species to selectively promote the activation of C–H and O–H bonds in methanol molecules.

[a]*School of Chemical Engineering, Australian Institute for Bioengineering and Nanotechnology, The University of Queensland, St Lucia, Brisbane, Queensland, 4072, Australia. E-mail: l.wang@uq.edu.au*

[b]*College of Physics, Hebei Key Laboratory of Photophysics Research and Application, Hebei Normal University, Shijiazhuang, Hebei Province, 050024, China*

[c]*CSIRO Mineral Resources, 1 Technology Court, Pullenvale, QLD, 4069, Australia*

[d]*Dept of Applied Biology and Chemical Technology, The Hong Kong Polytechnic University, Hung Hom, Kowloon, Hong Kong SAR*

Rhodium (Rh) is selected as a model because Rh is a high-performance HEC in photocatalytic overall water-splitting systems, yet the potential for methanol dehydrogenation has rarely been explored.[16–19] The RhO_x with mixed valence states of Rh (Rh^0, Rh^{3+}) on the surface of titanium dioxide (TiO_2, anatase, particle size < 25 nm) shows an H_2 evolution rate of 902.25 μmol h^{-1} with an apparent turnover frequency (TOF) of 1236 h^{-1}, superior to most reported co-catalysts. Characterizations reveal that the metallic Rh (Rh^0) species facilitate the C–H bond cleavage, and the oxidative Rh (Rh^{3+}) species favour the scission of the O–H bond in the methanol molecule. In addition, the synergy of Rh^0 and Rh^{3+} species is shown to aid the desorption of H_2 molecules. It is also probed that partially reduced palladium oxide (mixed Pd valence species) on TiO_2 (PdO_x/TiO_2) outperforms its oxide counterpart (PdO/TiO_2) for methanol dehydrogenation reaction, suggesting the generic feature of this multi-valence strategy.

Results and discussion

The preparation of photocatalysts began with the synthesis of rhodium oxide (Rh_2O_3) on TiO_2 (Rh_2O_3/TiO_2) using a molten-salt method.[10] For the three phases of TiO_2, it is widely discussed that anatase outperforms the other two phases (rutile

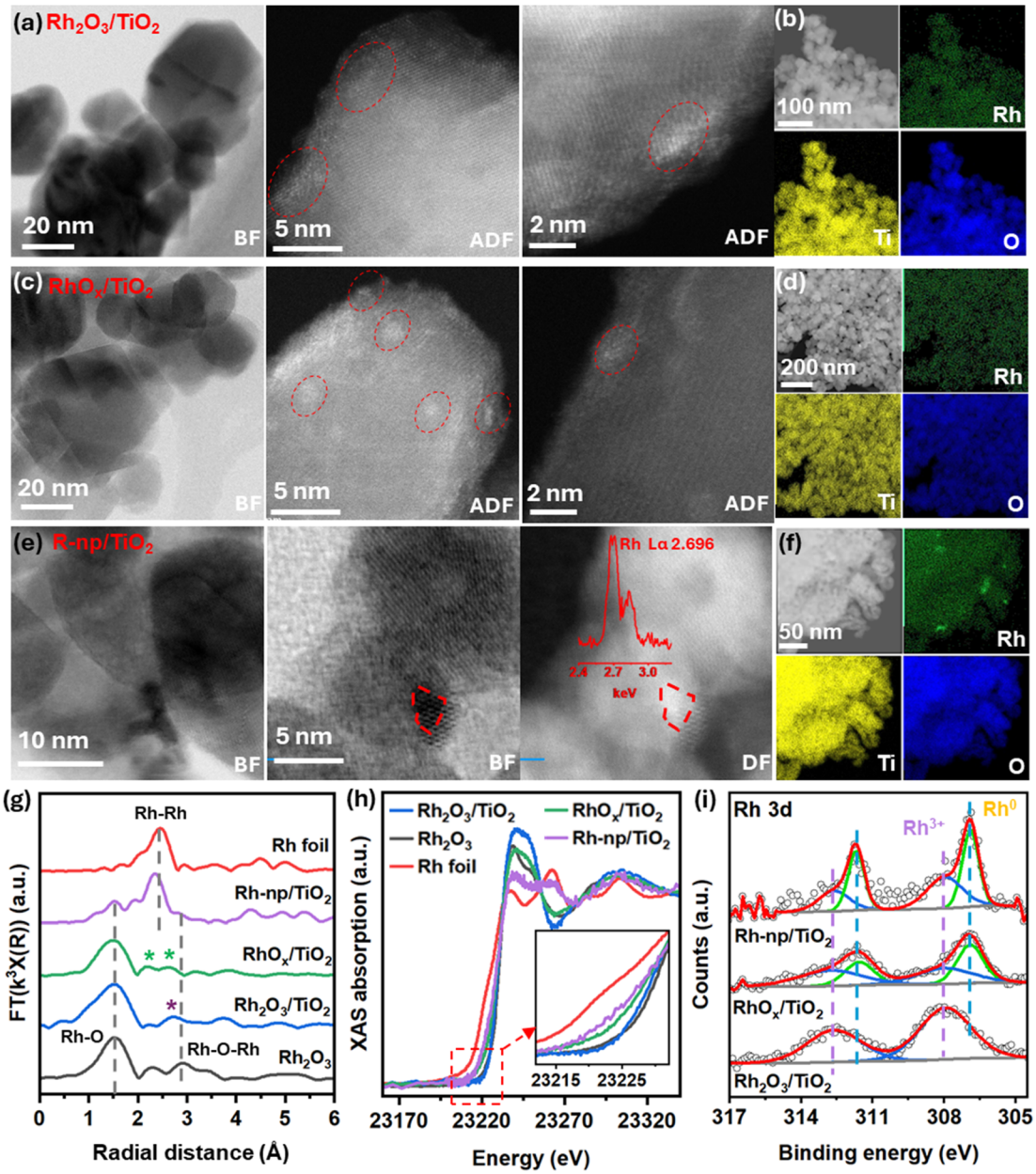

Fig. 1 Annular dark field (ADF), bright-field (BF) and dark-field (DF) STEM images, and EDS mapping of (a and b) Rh_2O_3/TiO_2; (c and d) RhO_x/TiO_2; (e and f) Rh-np/TiO_2, the inset is EDS spectrum of Rh; (g) Fourier transformed (FT) k^3-weighted $\chi(k)$ function of the EXAFS spectra, (h) XANES spectra recorded at the Rh-K edge, (i) XPS spectra of the Rh 3d for Rh_2O_3/TiO_2, RhO_x/TiO_2 and Rh-np/TiO_2.

and brookite) for photocatalysis.[20,21] Therefore, the TiO_2 anatase nanoparticles (<25 nm) are used in this work. Then the Rh species in Rh_2O_3/TiO_2 were partially reduced using a thermal treatment in the H_2 atmosphere, of which the obtained sample was denoted as RhO_x/TiO_2. The thermal treatment temperature and the Rh content were optimized to be 275 °C and 0.15 wt%, respectively (Fig. S1 and S2). In addition, the metallic Rh nanoparticle (Rh-np) decorated TiO_2 (Rh-np/TiO_2) was prepared as a reference using a conventional photo-deposition method.[22] The inductively coupled plasma optical emission spectroscopy measures the Rh contents in Rh_2O_3/TiO_2, RhO_x/TiO_2, and Rh-np/TiO_2 to be 0.142 wt%, 0.143 wt%, and 0.151 wt% (Table S1), respectively, which is close to the calculated value of 0.15 wt%. The morphology, crystal structure, and chemical state of the TiO_2 in Rh_2O_3/TiO_2, RhO_x/TiO_2, and Rh-np/TiO_2 photocatalysts were first characterized, and there were no significant differences found among these photocatalysts (Fig. S3–S6). The specific surface area of Rh-np/TiO_2, Rh_2O_3/TiO_2 and RhO_x/TiO_2 were 53.16 $m^2\ g^{-1}$, 53.19 $m^2\ g^{-1}$, 50.13 $m^2\ g^{-1}$, respectively. Compared to the original TiO_2, the enhanced light absorbance of Rh_2O_3/TiO_2, RhO_x/TiO_2, and Rh-np/TiO_2 at the visible-light range can be attributed to the Rh species (Fig. S7).

The bright species in high-resolution scanning transmission electron microscopy (STEM) images of Rh_2O_3/TiO_2 indicate the presence of Rh-based nanoclusters on the surface of TiO_2, which is further manifested by the element mapping images (Fig. 1a, b and S8).[23] After thermal treatment in H_2 atmosphere, the Rh-based nanoclusters transformed into ultrafine nanodots (<1 nm), as demonstrated by the STEM images of RhO_x/TiO_2. The molten-salt method can facilitate the monodispersing of metal species on the surface of TiO_2, thereby reducing the use of noble-metal co-catalysts.[10] In contrast, STEM images of Rh-np/TiO_2 display the existence of Rh nanoparticles with a size of around 3 nm, of which the Rh component was further evidenced by the energy-dispersive X-ray spectroscopy (EDS, Fig. 1e, f and S10). The Fourier transforms (FT) of the extended X-ray absorption fine structure (EXAFS) further demonstrate the local coordination of Rh species in these samples. Rh foil and Rh_2O_3 powder were included as references for the X-ray absorption spectroscopy (XAS), of which the peaks at 1.53 Å, 2.54 Å, and 2.91 Å can be allocated to Rh–O scattering, Rh–Rh scattering, and Rh–O–Rh scattering, respectively (Fig. 1g).[24,25] The high-intensity Rh–Rh peak in the EXAFS of Rh-np/TiO_2 confirms the aggregation of Rh atoms. A strong Rh–O peak (1.53 Å) and a weak Rh–O–Rh peak (2.73 Å) appear in the EXAFS of Rh_2O_3/TiO_2. In addition to the Rh–O peak, there are two peaks between 2.1 Å and 2.9 Å in the EXAFS of RhO_x/TiO_2, which can be related to the mixture of Rh–Rh and Rh–O–Rh bonds. The

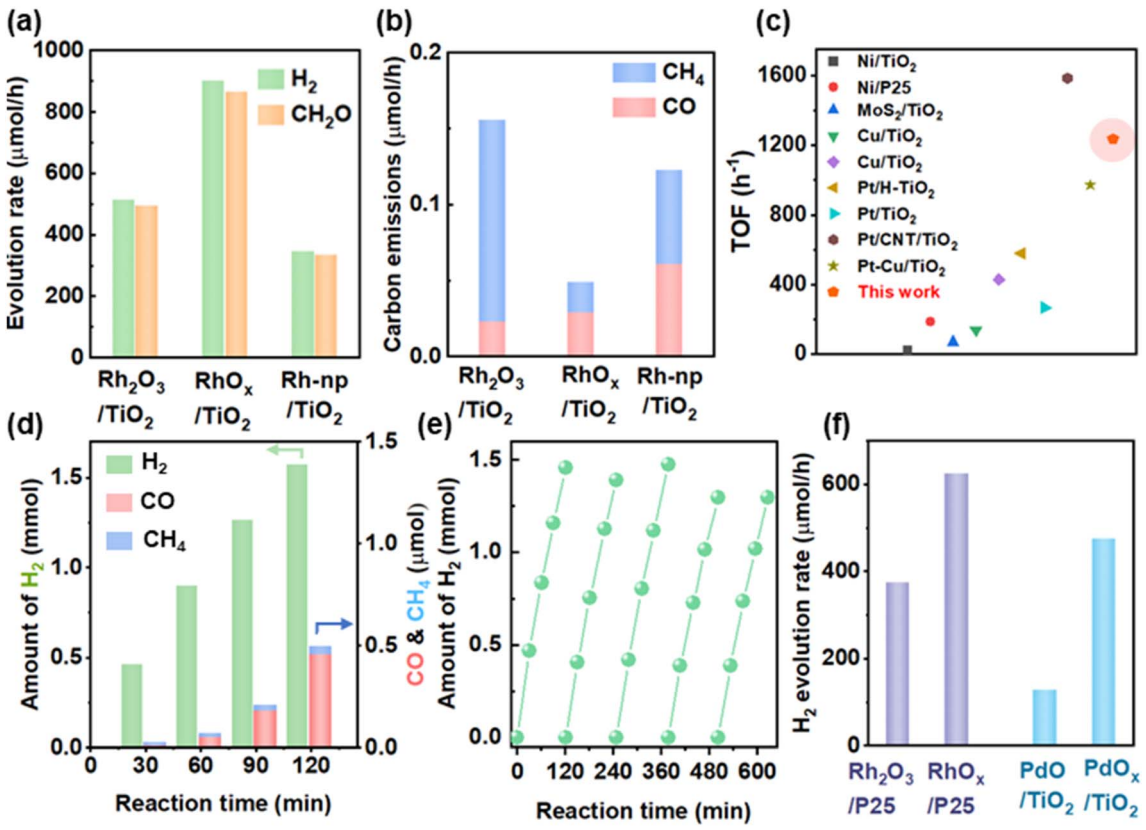

Fig. 2 (a) H_2 and CH_2O evolution rates; and (b) CO and CH_4 evolution rates of Rh_2O_3/TiO_2, RhO_x/TiO_2, and Rh-np/TiO_2 for photocatalytic methanol dehydrogenation. (c) Comparison of apparent TOF values in previous reported works with that of RhO_x/TiO_2 in this work.[5,9–11,34–38] (d and e) Cycling test of RhO_x/TiO_2 for photocatalytic methanol dehydrogenation. (f) Photocatalytic H_2 evolution rates of Rh_2O_3/P25, RhO_x/P25, PdO/TiO_2, and PdO_x/TiO_2. Photocatalytic measurement conditions: 50 mg of the photocatalyst dispersed in 50 mL of methanol (anhydrous, >99.8%) under mechanical stirring, 300 W Xe lamp (320–780 nm), 20 °C, 1 atm.

negative shift of the length of Rh–Rh and Rh–O–Rh scatterings can be attributed to the small size of Rh_2O_3, RhO_x, and Rh-np in these samples.[26] The combination of STEM images and EXAFS results suggests that Rh_2O_3 and RhO_x are most probably present as nanoclusters on the surface of TiO_2.

The valence states of Rh species in all photocatalysts were characterized using XAS and X-ray photoelectron spectroscopy (XPS). The X-ray absorption near-edge structure (XANES) of Rh_2O_3/TiO_2 overlaps with that of Rh_2O_3, manifesting the oxidized state of Rh species in the synthesized Rh_2O_3/TiO_2 (Fig. 1h).[27] The XANES of RhO_x/TiO_2 lies between that of Rh foil and Rh_2O_3/TiO_2, suggesting the partially reduced valence state of Rh species after the thermal treatment in the H_2 atmosphere. In addition, the XANES of Rh-np/TiO_2 is located between that of Rh foil and RhO_x/TiO_2, indicating a higher reduced state of Rh species in Rh-np/TiO_2 than that of RhO_x/TiO_2. It is also explored that XPS spectra of Rh 3d evidence the valence state of Rh species in these samples (Fig. 1i). Only Rh^{3+} was detected in Rh_2O_3/TiO_2, but Rh^0 and Rh^{3+} were found in RhO_x/TiO_2 and Rh-np/TiO_2. The co-existence of Rh^0 and Rh^{3+} in Rh-np/TiO_2 can be attributed to the partial oxidation of photo-deposited Rh nanoparticles when exposed to air.[28,29] Accordingly, the primary Rh^{3+} species in RhO_x/TiO_2 are proposed to stay on the surface of the RhO_x nanocluster, of which the distribution may also be influenced by the surface structure of TiO_2.[30] The XPS analysis also shows that the $Rh^{3+}/(Rh^0 + Rh^{3+})$ ratio of RhO_x/TiO_2 is 52.84%, which is slightly higher than that of Rh-np/TiO_2 (42.93%), consistent with the XANES result.

The influence of Rh species on the methanol dehydrogenation processes was probed by evaluating the photocatalytic performance of Rh_2O_3/TiO_2, RhO_x/TiO_2, and Rh-np/TiO_2 photocatalysts. Anhydrous methanol (>99.8%) rather than methanol aqueous solution is selected as the reaction solution to suppress the CO_2 generation ($CH_3OH + H_2O \rightarrow 3H_2 + CO_2$).[31] The H_2 and formaldehyde are the major products, with trace amounts of carbon monoxide (CO) and methane (CH_4) detected in the reactions using all these photocatalysts (Fig. 2a and b). There may be a trace amount of CO_2 produced due to the absorbed water in methanol.[31] The CO can be generated from the complete dehydrogenation of methanol, while the formation of CH_4 can be caused by the hydrogenation of methanol intermediates.[32] These results manifest the high selectivity of Rh species as co-catalysts toward the production of formaldehyde for photocatalytic methanol dehydrogenation reactions. The high selectivity toward formaldehyde may be attributed to favorable kinetics on Rh species because the production of CO possesses a lower Gibbs free energy difference ($\Delta G^{\circ}_{298} = 20.9$ kJ mol^{-1}) than the production of formaldehyde ($\Delta G^{\circ}_{298} = 63.5$ kJ mol^{-1}).[33] In particular, RhO_x/TiO_2 shows the highest H_2 evolution rate (902.25 μmol h^{-1}) among these three samples, which is 75% and 161% over that of Rh_2O_3/TiO_2 and Rh-np/TiO_2, respectively. An apparent TOF of 1236 h^{-1} was achieved with the RhO_x/TiO_2 photocatalyst, outperforming that of most reported co-catalysts for photocatalytic methanol dehydrogenation (Fig. 2c and Table S2). The optimal photocatalytic system reached an apparent quantum efficiency of 18% at 380 nm. There was no obvious decay of the H_2 evolution rate on RhO_x/TiO_2 observed in five successive photocatalysis cycles, highlighting the cycling durability of the RhO_x/TiO_2 photocatalyst (Fig. 2d and e). The STEM, XANES, EXAFS, and element analysis results of RhO_x/TiO_2 after the photocatalytic test further confirm the structural and compositional stability of this photocatalyst (Fig. S11–S13). It is worth noting that there may be reversible charge transfer between the photocatalyst and methanol under light illumination, which can induce the change of the Rh valence state in these photocatalysts.[5] In addition, a similar tendency was observed when replacing anatase-phase TiO_2 with P25 (mixed phases of anatase and rutile, 21 nm) or replacing Rh species with Pd species (Fig. 2f), indicating the universality of this multi-valence strategy for methanol dehydrogenation reaction.

Although insignificant structural properties of TiO_2 were detected in RhO_x/TiO_2. Rh_2O_3/TiO_2, and Rh-np/TiO_2 photocatalysts, control samples were prepared to investigate the impact of synthetic procedures on the photocatalytic activity of TiO_2. The initial TiO_2 went through the molten salt synthesis and hydrogen thermal treatment without Rh species, which were denoted as TiO_2_MS and TiO_2_MS_H, respectively. The Rh-np/TiO_2_MS and Rh-np/TiO_2_MS_H showed similar photocatalytic performance as Rh-np/TiO_2 (Table S3). Meanwhile, there are no obvious changes in the valence states of Rh species

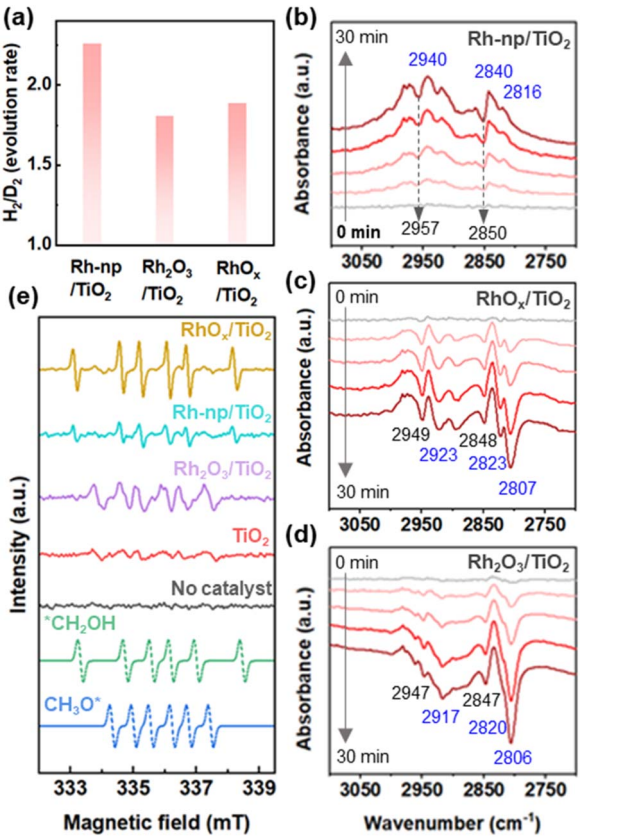

Fig. 3 (a) KIE measurement, (b–d) gas-phase *in situ* DRIFTS spectra, and (e) *in situ* EPR spectra of Rh-np/TiO_2, RhO_x/TiO_2, and Rh_2O_3/TiO_2, respectively. The dashed lines in (e) represent the simulated spectra of CH_3O* and *CH_2OH radicals.

in Rh_2O_3/TiO_2 and RhO_x/TiO_2 that can be detected after the photocatalytic test (Fig. S14). Therefore, the distinct photocatalytic performances of these photocatalysts can be attributed to the Rh species in these materials. To verify this hypothesis, the kinetic isotope effect (KIE) was measured to evaluate the catalytic capability of Rh-based co-catalysts in these photocatalysts, which is demonstrated by the ratio of the H_2 evolution rate from methanol (CH_3OH) and D_2 evolution rate from methanol-d_4 (CD_3OD).[39] Generally, heavier isotopes require greater energy input to reach the transition state of the reaction, resulting in a slower reaction rate and a KIE value over one.[40] Here, the KIE values are calculated to be 2.60, 1.89, and 1.82 for Rh-np/TiO_2, RhO_x/TiO_2, and Rh_2O_3/TiO_2, respectively (Fig. 3a). The much lower KIE value of RhO_x/TiO_2 than that of Rh-np/TiO_2 indicates that RhO_x works better for activating methanol molecules than Rh-np, which can enhance photocatalytic productivity.[39] Interestingly, the KIE value of Rh_2O_3/TiO_2 is slightly lower than that of RhO_x/TiO_2, but the latter shows a higher H_2 evolution rate for photocatalytic methanol dehydrogenation. Therefore, there should be other factors that affect the catalytic activity of these photocatalysts. Advanced *in situ* techniques were applied to investigate the mechanism of the methanol dehydrogenation processes on Rh_2O_3/TiO_2, RhO_x/TiO_2, and Rh-np/TiO_2 below.

The *in situ* diffuse reflectance infrared Fourier transform spectroscopy (DRIFTS) measurement was conducted to track possible reaction intermediates of methanol dehydrogenation on these photocatalysts. The negative peaks of CH_3OH adsorbates present on Rh-np/TiO_2 (2850 cm^{-1} and 2957 cm^{-1}), RhO_x/TiO_2 (2848 cm^{-1} and 2949 cm^{-1}), and Rh_2O_3/TiO_2 (2847 cm^{-1} and 2947 cm^{-1}) under light irradiation, suggesting the conversion of methanol on these photocatalysts (Fig. 3b–d).[41–43] The positive peaks at 2940 cm^{-1}, 2840 cm^{-1}, and 2816 cm^{-1} indicate the accumulation of methoxy (CH_3O^*) adsorbates on Rh-np/TiO_2, while the corresponding negative peaks on RhO_x/TiO_2 (2923 cm^{-1}, 2823 cm^{-1}, and 2807 cm^{-1}) and Rh_2O_3/TiO_2 (2917 cm^{-1}, 2820 cm^{-1}, and 2806 cm^{-1}) demonstrate the consumption of CH_3O^* adsorbates.[41] In addition, DRIFTS spectra of TiO_2 show a slight accumulation of CH_3O^* (2826 cm^{-1}) on the surface (Fig. S15). These results manifest that the RhO_x/TiO_2 and Rh_2O_3/TiO_2 are more effective than Rh-np/TiO_2 for the activation of methanol molecules, which is consistent with KIE values. In particular, the sharp peaks of CH_3O^* adsorbate on Rh_2O_3/TiO_2 suggest significant dissociative adsorption of methanol molecules *via* the cleavage of the O–H bond (Fig. 3d).

Since the conversion of methanol molecules can begin with the scission of either the O–H bond or C–H bond, there are two possible pathways for the methanol conversion to produce H_2 and formaldehyde (eqn (1) and (2)).[7] Accordingly, hydroxyl methyl ($^*CH_2OH$) and CH_3O^* radicals can be generated as reaction intermediates in pathway I and pathway II, respectively.[44] The detection of possible radicals was then conducted using the *in situ* electron paramagnetic resonance (EPR) spectroscopy. The signal belonging to $^*CH_2OH$ was predominant for RhO_x/TiO_2 and Rh-np/TiO_2, while only CH_3O^* was detected for Rh_2O_3/TiO_2 (Fig. 3e and S16).[44] Different methanol intermediates suggest different reaction pathways for Rh_2O_3/TiO_2, $RhO_x/$

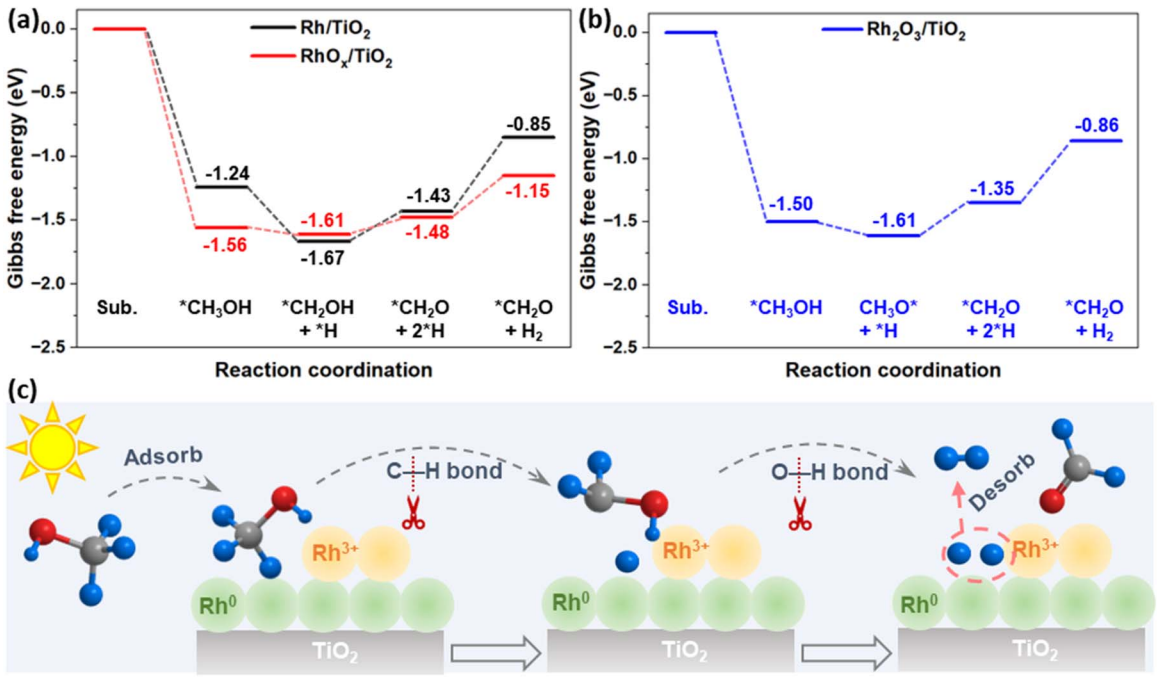

Fig. 4 Computational calculations of the Gibbs free energy profiles for methanol conversion to produce H_2 and formaldehyde (CH_2O) *via* (a) pathway I on Rh/TiO_2 and RhO_x/TiO_2, (b) pathway II on Rh_2O_3/TiO_2. (c) Scheme of the proposed mechanism for the photocatalytic methanol dehydrogenation to produce H_2 and formaldehyde on RhO_x/TiO_2. The grey, red, and blue balls represent carbon (C), oxygen (O), and hydrogen (H) atoms, respectively.

TiO_2, and Rh-np/TiO_2. It is most possible that the methanol conversion takes place with the cleavage of the C–H bond in the methanol molecule on RhO_x/TiO_2 and Rh-np/TiO_2 (pathway I), while Rh_2O_3/TiO_2 goes to scissor the O–H bond of the methanol molecule as the first step (pathway II).[7] These suggested reaction pathways warrant the following investigation of the mechanism with the aid of computational calculations.

$$\text{Pathway I: } CH_3OH \rightarrow *CH_2OH + H^* \rightarrow CH_2O^* + 2H^* \rightarrow CH_2O + H_2 \quad (1)$$

$$\text{Pathway II: } CH_3OH \rightarrow CH_3O^* + H^* \rightarrow CH_2O^* + 2H^* \rightarrow CH_2O + H_2 \quad (2)$$

Computational calculations were conducted to better understand the mechanism of different reaction pathways on metallic Rh (Rh/TiO_2), a mixture of metallic Rh and oxidative Rh species (RhO_x/TiO_2), and oxidative Rh (Rh_2O_3/TiO_2) on the surface of TiO_2 (Fig. S17–S19).[45] According to the free Gibbs energy profiles, the scission of the C–H bond and O–H bond as the first step proceeds spontaneously on Rh/TiO_2 and Rh_2O_3/TiO_2, respectively, while both photocatalysts face a high free energy barrier (>0.2 eV) for the second step (Fig. 4a and b). The RhO_x/TiO_2 shows a much lower free energy barrier (0.13 eV) for the cleavage of the O–H bond as the second step, compared to that (0.24 eV) of Rh/TiO_2, thus promoting the methanol dehydrogenation process. It is also shown that the free energy barrier for the desorption of H_2 is in the order of Rh/TiO_2 (0.58 eV) > Rh_2O_3/TiO_2 (0.49 eV) > RhO_x/TiO_2 (0.33 eV), which indicates the beneficial role of multi-valence Rh species for the H_2 desorption. Based on these results and analysis, a mechanism is proposed for the superior photocatalytic performance of RhO_x/TiO_2 (Fig. 4c). The photocatalytic conversion of methanol on RhO_x/TiO_2 starts with the C–H bond cleavage on Rh^0 species, followed by the breaking of the O–H bond on Rh^{3+} species. Finally, the generated protons on Rh^0 and Rh^{3+} recombine to release H_2 molecules. The methanol oxidation reaction likely takes place on Rh^{3+} to produce HCHO, and the protons are reduced on Rh^0 to generate H_2.[5] The cooperation of Rh^0 and Rh^{3+} species not only facilitates the scission of C–H and O–H bonds in methanol molecules but also aids the desorption of H_2 molecules. The facile desorption of H_2 molecules can enable the fast recovery of the catalytic active site for the next reaction cycle, while the liquid environment may also affect the H_2 desorption in practice.

Conclusions

Through the design of multi-valence metal species in the co-catalysts, this work develops an effective strategy for engineering materials to promote photocatalytic methanol dehydrogenation processes. In the case study of the RhO_x/TiO_2 photocatalyst, it is suggested that the oxidative Rh and metallic Rh species promote the scission of the O–H and C–H bonds in methanol molecules, respectively. Moreover, the mixture of oxidative Rh and metallic Rh species boosts the desorption of H_2 molecules, which is essential for the fast recovery of active sites for the next reaction cycle. This synergy of multi-valent Rh species in RhO_x/TiO_2 photocatalyst results in an apparent TOF of 1236 h^{-1}, exceeding that of most reported co-catalysts. In addition, this strategy can be extended to Pd species, of which the PdO_x/TiO_2 delivers significantly improved performance compared to PdO/TiO_2 for photocatalytic methanol dehydrogenation reaction, showing its certain universality. The unveiled mechanism is expected to inspire the catalyst design for promoting the conversion of primary alcohols to value-added fuels and chemicals.

Author contributions

All authors contributed to the draft of this manuscript and have approved the final version of the manuscript. M. Xiao and L. Wang conceived the project. W. Meng and Y. Jiao conducted the computational study. H. Lu assisted with the XAS measurement. G. Zhao and Y. Jin supported the DRIFTS characterisations. Zitong Wang collected the XPS data.

Conflicts of interest

There are no conflicts to declare.

Data availability

The datasets generated during and/or analysed during the current study are not publicly available due to restrictions applied to the availability of these data but are available from the authors on reasonable request.

SI is available and includes experimental procedures, characterization data of the materials (XRD, XPS, SEM, TEM, DRIFTS, EPR, UV-vis, XAS) and computational details. See DOI: https://doi.org/10.1039/d5ra05449d.

Acknowledgements

The authors acknowledge the financial support from the Australian Research Council (ARC) through the Discovery Project (DP230100621), Laureate Fellowship (FL190100139), and Discovery Early Career Researcher Award (DE240100810). M. X. acknowledges the Philanthropic Grant (RM 2022002231) supported by the faculty of Engineering, Architecture, and Information Technology (EAIT) at the University of Queensland (UQ). M. X. thanks the technical support from the Centre for Microscopy and Microanalysis (CMM) and the Centre for Advanced Imaging (CAI), UQ. This research was undertaken on the X-ray Absorption Spectroscopy beamline at the Australian Synchrotron, part of ANSTO. M. X. expresses gratitude for the electronic microscopy support from Dr Nadja Tarakina and Miss Bolortuya Badamdorj at the Max Planck Institute of Colloids and Interfaces, Germany. The collection of experimental data and insightful discussion from Dr Miaoqiang Lyu is appreciated.

References

1 C. F. Shih, T. Zhang, J. Li and C. Bai, *Joule*, 2018, **2**, 1925–1949.
2 D. R. Palo, R. A. Dagle and J. D. Holladay, *Chem. Rev.*, 2007, **107**, 3992–4021.
3 L. E. Heim, H. Konnerth and M. H. G. Prechtl, *Green Chem.*, 2017, **19**, 2347–2355.
4 K. Z. Gaca, J. A. Parkinson, L. Lue and J. Sefcik, *Ind. Eng. Chem. Res.*, 2014, **53**, 9262–9271.
5 H. Wang, H. Qi, X. Sun, S. Jia, X. Li, T. J. Miao, L. Xiong, S. Wang, X. Zhang, X. Liu, A. Wang, T. Zhang, W. Huang and J. Tang, *Nat. Mater.*, 2023, **22**, 619–626.
6 N. Uddin, Z. Sun, J. Langley, H. Lu, P. Cao, A. Wibowo, X. Yin, C. S. Tang, H. T. Nguyen, J. D. Evans, X. Li, X. Zhang, M. Heggen, R. E. Dunin-Borkowski, A. T. S. Wee, H. Zhao, N. Cox and Z. Yin, *Proc. Natl. Acad. Sci. U. S. A.*, 2023, **120**, e2212075120.
7 Y. Pang, M. N. Uddin, W. Chen, S. Javaid, E. Barker, Y. Li, A. Suvorova, M. Saunders, Z. Yin and G. Jia, *Adv. Mater.*, 2019, **31**, 1905540.
8 M. Xiao, Z. Wang, M. Lyu, B. Luo, S. Wang, G. Liu, H.-M. Cheng and L. Wang, *Adv. Mater.*, 2019, **31**, 1801369.
9 Y. Zhang, J. Zhao, H. Wang, B. Xiao, W. Zhang, X. Zhao, T. Lv, M. Thangamuthu, J. Zhang, Y. Guo, J. Ma, L. Lin, J. Tang, R. Huang and Q. Liu, *Nat. Commun.*, 2022, **13**, 58.
10 M. Xiao, L. Zhang, B. Luo, M. Lyu, Z. Wang, H. Huang, S. Wang, A. Du and L. Wang, *Angew. Chem., Int. Ed.*, 2020, **59**, 7230–7234.
11 Y.-J. Yuan, Z.-J. Ye, H.-W. Lu, B. Hu, Y.-H. Li, D.-Q. Chen, J.-S. Zhong, Z.-T. Yu and Z.-G. Zou, *ACS Catal.*, 2016, **6**, 532–541.
12 L.-N. Chen, K.-P. Hou, Y.-S. Liu, Z.-Y. Qi, Q. Zheng, Y.-H. Lu, J.-Y. Chen, J.-L. Chen, C.-W. Pao, S.-B. Wang, Y.-B. Li, S.-H. Xie, F.-D. Liu, D. Prendergast, L. E. Klebanoff, V. Stavila, M. D. Allendorf, J. Guo, L.-S. Zheng, J. Su and G. A. Somorjai, *J. Am. Chem. Soc.*, 2019, **141**, 17995–17999.
13 L. Chen, Z. Qi, X. Peng, J.-L. Chen, C.-W. Pao, X. Zhang, C. Dun, M. Young, D. Prendergast, J. J. Urban, J. Guo, G. A. Somorjai and J. Su, *J. Am. Chem. Soc.*, 2021, **143**, 12074–12081.
14 A. Kaithal, B. Chatterjee, C. Werlé and W. Leitner, *Angew. Chem., Int. Ed.*, 2021, **60**, 26500–26505.
15 Y. Hao, D. Yu, S. Zhu, C.-H. Kuo, Y.-M. Chang, L. Wang, H.-Y. Chen, M. Shao and S. Peng, *Energy Environ. Sci.*, 2023, **16**, 1100–1110.
16 K. Maeda, K. Teramura, D. Lu, N. Saito, Y. Inoue and K. Domen, *Angew. Chem., Int. Ed.*, 2006, **45**, 7806–7809.
17 M. Liu, G. Zhang, X. Liang, Z. Pan, D. Zheng, S. Wang, Z. Yu, Y. Hou and X. Wang, *Angew. Chem., Int. Ed.*, 2023, **62**, e202304694.
18 T. Takata, J. Jiang, Y. Sakata, M. Nakabayashi, N. Shibata, V. Nandal, K. Seki, T. Hisatomi and K. Domen, *Nature*, 2020, **581**, 411–414.
19 S. Ida, K. Sato, T. Nagata, H. Hagiwara, M. Watanabe, N. Kim, Y. Shiota, M. Koinuma, S. Takenaka, T. Sakai, E. Ertekin and T. Ishihara, *Angew. Chem., Int. Ed.*, 2018, **57**, 9073–9077.
20 J. Zhang, P. Zhou, J. Liu and J. Yu, *Phys. Chem. Chem. Phys.*, 2014, **16**, 20382–20386.
21 W. Kim, T. Tachikawa, G.-h. Moon, T. Majima and W. Choi, *Angew. Chem., Int. Ed.*, 2014, **53**, 14036–14041.
22 K. Wenderich and G. Mul, *Chem. Rev.*, 2016, **116**, 14587–14619.
23 K. Khivantsev, C. G. Vargas, J. Tian, L. Kovarik, N. R. Jaegers, J. Szanyi and Y. Wang, *Angew. Chem., Int. Ed.*, 2021, **60**, 391–398.
24 F. Gu, X. Qin, M. Li, Y. Xu, S. Hong, M. Ouyang, G. Giannakakis, S. Cao, M. Peng, J. Xie, M. Wang, D. Han, D. Xiao, X. Wang, Z. Wang and D. Ma, *Angew. Chem., Int. Ed.*, 2022, **61**, e202201540.
25 L. Zeng, Y. Chen, M. Sun, Q. Huang, K. Sun, J. Ma, J. Li, H. Tan, M. Li, Y. Pan, Y. Liu, M. Luo, B. Huang and S. Guo, *J. Am. Chem. Soc.*, 2023, **145**, 17577–17587.
26 J. T. Miller, A. J. Kropf, Y. Zha, J. R. Regalbuto, L. Delannoy, C. Louis, E. Bus and J. A. van Bokhoven, *J. Catal.*, 2006, **240**, 222–234.
27 Y. Liu, J. Ding, F. Li, X. Su, Q. Zhang, G. Guan, F. Hu, J. Zhang, Q. Wang, Y. Jiang, B. Liu and H. B. Yang, *Adv. Mater.*, 2023, **35**, 2207114.
28 S. Liu, Y. Ji, S. Yang, L. Li, Q. Shao, Z. Hu, C.-W. Pao, J.-L. Chen, T.-S. Chan, T. Zhu, Y. Li, X. Huang and J. Lu, *Chem Catal.*, 2021, **1**, 1104–1117.
29 K. Teramura, S.-i. Okuoka, S. Yamazoe, K. Kato, T. Shishido and T. Tanaka, *J. Phys. Chem. C*, 2008, **112**, 8495–8498.
30 P. Winkler, J. Zeininger, M. Raab, Y. Suchorski, A. Steiger-Thirsfeld, M. Stöger-Pollach, M. Amati, L. Gregoratti, H. Grönbeck and G. Rupprechter, *Nat. Commun.*, 2021, **12**, 6517.
31 M. Xiao, A. Baktash, M. Lyu, G. Zhao, Y. Jin and L. Wang, *Angew. Chem., Int. Ed.*, 2024, **63**, e202402004.
32 Z. Zhao, X. Yao and G. Hou, *ACS Catal.*, 2023, **13**, 7978–7986.
33 E. Alberico and M. Nielsen, *Chem. Commun.*, 2015, **51**, 6714–6725.
34 W.-T. Chen, A. Chan, D. Sun-Waterhouse, J. Llorca, H. Idriss and G. I. N. Waterhouse, *J. Catal.*, 2018, **367**, 27–42.
35 B.-H. Lee, S. Park, M. Kim, A. K. Sinha, S. C. Lee, E. Jung, W. J. Chang, K.-S. Lee, J. H. Kim, S.-P. Cho, H. Kim, K. T. Nam and T. Hyeon, *Nat. Mater.*, 2019, **18**, 620–626.
36 X. Ruan, X. Cui, Y. Cui, X. Fan, Z. Li, T. Xie, K. Ba, G. Jia, H. Zhang, L. Zhang, W. Zhang, X. Zhao, J. Leng, S. Jin, D. J. Singh and W. Zheng, *Adv. Energy Mater.*, 2022, **12**, 2200298.
37 S. Rej, S. M. H. Hejazi, Z. Badura, G. Zoppellaro, S. Kalytchuk, Š. Kment, P. Fornasiero and A. Naldoni, *ACS Sustain. Chem. Eng.*, 2022, **10**, 17286–17296.
38 A. Moya, A. Cherevan, S. Marchesan, P. Gebhardt, M. Prato, D. Eder and J. J. Vilatela, *Appl. Catal., B*, 2015, **179**, 574–582.
39 S. Luo, H. Lin, Q. Wang, X. Ren, D. Hernández-Pinilla, T. Nagao, Y. Xie, G. Yang, S. Li, H. Song, M. Oshikiri and J. Ye, *J. Am. Chem. Soc.*, 2021, **143**, 12145–12153.
40 X. Wang, D. Li, Z. Gao, Y. Guo, H. Zhang and D. Ma, *J. Am. Chem. Soc.*, 2023, **145**, 905–918.

41 Z. Qi, L. Chen, S. Zhang, J. Su and G. A. Somorjai, *J. Am. Chem. Soc.*, 2021, **143**, 60–64.
42 C. Fu, F. Li, J. Zhang, D. Li, K. Qian, Y. Liu, J. Tang, F. Fan, Q. Zhang, X.-Q. Gong and W. Huang, *Angew. Chem., Int. Ed.*, 2021, **60**, 6160–6169.
43 G. L. Chiarello, D. Ferri and E. Selli, *Appl. Surf. Sci.*, 2018, **450**, 146–154.
44 K. Kočí, M. Reli, M. Edelmannová, I. Troppová, H. Drobná, A. Rokicińska, P. Kuśtrowski, D. Dvoranová and L. Čapek, *J. Photochem. Photobiol., A*, 2018, **366**, 55–64.
45 W. Chen, E. D. Cubuk, M. M. Montemore, C. Reece, R. J. Madix, C. M. Friend and E. Kaxiras, *J. Phys. Chem. C*, 2018, **122**, 7806–7815.